

Article

AACVD of Cu₃N on Al₂O₃ Using CuCl₂ and NH₃

Matthew Zervos

Nanostructured Materials and Devices Laboratory, School of Engineering, University of Cyprus, P.O. Box 20537, Nicosia 1678, Cyprus; zervos@ucy.ac.cy

Abstract: Cu₃N has been grown on m-Al₂O₃ by aerosol-assisted chemical vapor deposition using 0.1 M CuCl₂ in CH₃CH₂OH under an excess of NH₃ at 600 °C, which led to the deposition of Cu that was subsequently converted into Cu₃N under NH₃: O₂ at 400 °C in a two-step process without exposure to the ambient. The reaction of CuCl₂ with an excess of NH₃ did not lead to the growth of Cu₃N, which is different to the case of halide vapor phase epitaxy of III-V semiconductors. The Cu₃N layers obtained in this way had an anti-ReO₃ cubic crystal structure with a lattice constant of 3.8 Å and were found to be persistently n-type, with a room temperature carrier density of $n = 2 \times 10^{16} \text{ cm}^{-3}$ and mobility of $\mu_n = 32 \text{ cm}^2/\text{Vs}$. The surface depletion, calculated in the effective mass approximation, was found to extend over $\sim 0.15 \mu\text{m}$ by considering a surface barrier height of $\phi_B = 0.4 \text{ eV}$ related to the formation of native Cu₂O.

Keywords: copper nitride; chemical vapor deposition; structural; electrical properties

1. Introduction

Cu₃N is a novel semiconductor in which crystal imperfections such as Cu interstitials (Cu_i) and nitrogen vacancies (V_N) give rise to states that are energetically located inside or very close to the conduction and valence bands, respectively [1], but do not give rise to any mid-gap states. Consequently, it has been suggested to be suitable as a solar cell absorber in view of the fact that it has an indirect energy band gap of $\sim 1.0 \text{ eV}$ [2], but also due to the fact that n- and p-type doping are possible. However, despite the fact that Cu₃N has been described as a defect-tolerant semiconductor, so far no one has fabricated a working p-n junction solar cell using Cu₃N. In the past, Chen et al. [3] fabricated a Cu₃N p-n homojunction on indium tin oxide, and Yee et al. [1] fabricated an Al: ZnO/ZnS/Cu₃N p-n heterojunction, both of which exhibited rectifying behavior but no photogenerated current. This has been attributed to the large concentration of Cu_i defects, which capture electrons and result into substantial Shockley–Read–Hall recombination and quenching of the steady-state minority carrier concentration under illumination. In other words, crystal imperfections such as V_N and Cu_i can still reduce the minority carrier lifetime and prevent the extraction of photogenerated electron–hole pairs in Cu₃N. Nevertheless, Cu₃N has been used successfully for energy storage as it has a cubic anti-ReO₃ crystal structure, belonging to the Pm3m space group (number 221) with a lattice constant of 3.8 Å [4], and a vacant body center that can readily act as a host for Li ions in batteries [5]. Cu₃N has been obtained by many different methods including reactive sputtering [6], molecular beam epitaxy [7], atomic layer deposition [8,9] and pulsed laser deposition [10,11]. Recently, we converted Cu into Cu₃N under NH₃: O₂ between 400 °C and 600 °C, and observed distinct spectral features and maxima in differential transmission at 500 nm ($\equiv 2.48 \text{ eV}$), 550 nm ($\equiv 2.25 \text{ eV}$), 630 nm ($\equiv 1.97 \text{ eV}$) and 670 nm ($\equiv 1.85 \text{ eV}$) on a ps time scale by ultrafast pump–probe spectroscopy (UPPS) [12]. These correspond to the M and R direct energy band gaps of bulk-relaxed and strained Cu₃N in excellent agreement with density functional theory (DFT) calculations of the electronic band structure [12]. This observation of the M and R direct energy band gaps in fact confirmed that Cu₃N has a clean energy band gap. More recently, we also showed that iodine-doped Cu₃N, i.e., I: Cu₃N, is a p-type semiconductor and that



Citation: Zervos, M. AACVD of Cu₃N on Al₂O₃ Using CuCl₂ and NH₃. *Materials* **2022**, *15*, 8966. <https://doi.org/10.3390/ma15248966>

Academic Editor: Roberta G. Toro

Received: 1 October 2022

Accepted: 14 December 2022

Published: 15 December 2022

Publisher's Note: MDPI stays neutral with regard to jurisdictional claims in published maps and institutional affiliations.



Copyright: © 2022 by the author. Licensee MDPI, Basel, Switzerland. This article is an open access article distributed under the terms and conditions of the Creative Commons Attribution (CC BY) license (<https://creativecommons.org/licenses/by/4.0/>).

the extensive incorporation of I in Cu_3N can be used to convert Cu_3N into $\gamma\text{-CuI}$, which is a p-type transparent semiconductor that was used in conjunction with n-type Cu_3N , for the fabrication of a $\gamma\text{-CuI/TiO}_2/\text{Cu}_3\text{N}$ p-n heterojunction that exhibited rectifying current–voltage characteristics [13]. In the past, most have focused on n-type doping of Cu_3N , such as Gao et al. [14], who showed that the incorporation of Zn resulted into n-type Cu_3N and increased the carrier density from $n = 10^{17}$ to 10^{21} cm^{-3} with a resistivity of $10^{-3} \Omega \text{ cm}$. In contrast, only a few have considered p-type doping of Cu_3N , such as Matsuzaki et al. [15], who used NF_3 for the growth of F-doped p-type Cu_3N . The ability to obtain p-type Cu_3N is important, of course, for the realization of p-n junctions, but it should be noted that I-VII γ -cuprous halides such as $\gamma\text{-CuCl}$, CuBr and CuI are p-type transparent semiconductors with a zinc blende crystal structure and direct energy band-gaps of 3.3, 2.9 and 2.95 eV, respectively. In addition, they have lattice constants close to that of Si [16] and may be readily combined with Cu_3N for the realization of novel cuprous electronic and optoelectronic devices.

Here Cu_3N has been obtained by aerosol-assisted chemical vapor deposition (AACVD) using CuCl_2 in $\text{CH}_3\text{CH}_2\text{OH}$ and NH_3 . AACVD is a low-cost growth method [17] that has been used for the growth of a broad range of semiconductors [18] including III-V semiconductors such as InN , GaN and $\text{In}_x\text{Ga}_{1-x}\text{N}$ [19]. The growth of these III-Vs is carried out using anhydrous N_2 and NH_3 , i.e., O_2 and H_2O are generally avoided and eliminated. In the past, McInnes et al. [19] used 0.1M GaCl_3 and 0.1M InCl_3 in acetonitrile (CH_3CN), N_2 as carrier gas and anhydrous NH_3 to grow $\text{In}_x\text{Ga}_{1-x}\text{N}$. The total flow rate through the 0.1 M GaCl_3 and 0.1 M InCl_3 solutions was maintained at 529 mL min^{-1} , and anhydrous NH_3 was used at a high flow rate of 862 mL min^{-1} , which assisted in promoting the formation of smaller droplets whilst also ensuring an excess of NH_3 for the deposition of $\text{In}_x\text{Ga}_{1-x}\text{N}$. The deposition was carried out at $600 \text{ }^\circ\text{C}$, which exceeds the melting point of both GaCl_3 and InCl_3 and gave layers with a thickness of $\sim 2 \mu\text{m}$. Both GaCl_3 and InCl_3 react directly with NH_3 , leading to the deposition of GaN and InN , respectively, while CH_3CN [20] breaks into HCN and CH_4 at elevated temperatures [21,22].

AACVD has also been used for the growth of Cu_3N by Yamaguchi et al. [23], who obtained Cu_3N on $\alpha\text{-Al}_2\text{O}_3$ by AACVD at $300 \text{ }^\circ\text{C}$ using copper (II) acetylacetonate $\text{Cu}(\text{O}_2\text{C}_5\text{H}_7)_2$ that was dissolved in aqueous NH_3 . No CuO or Cu_2O was detected in the Cu_3N despite the fact that $\text{Cu}(\text{O}_2\text{C}_5\text{H}_7)_2$ was used in aqueous NH_3 . Others such as Park et al. [8] used metal organic sources of copper such as $\text{C}_{14}\text{H}_{32}\text{CuN}_2\text{O}_2$, which contains oxygen in conjunction with NH_3 for the atomic layer deposition of Cu_3N , but metal organic sources are expensive [9].

No one has previously attempted to grow Cu_3N using CuCl_2 and NH_3 by AACVD or tried to grow Cu_3N on $m\text{-Al}_2\text{O}_3$, which is ideally suited for the growth of cubic and tetragonal crystals. It is found that the reaction of CuCl_2 with NH_3 will not give Cu_3N as in the case of halide vapor phase epitaxy (HVPE) of III-V semiconductors such as $\text{In}_x\text{Ga}_{1-x}\text{N}$. In contrast, the reaction of CuCl_2 with an excess of NH_3 resulted into the deposition of polycrystalline Cu layers consisting of oriented grains on $m\text{-Al}_2\text{O}_3$, which have a higher crystal quality compared to Cu obtained by sputtering [12] or electron beam evaporation [15] used previously to obtain Cu_3N under $\text{NH}_3: \text{O}_2$. Consequently, the Cu layers on $m\text{-Al}_2\text{O}_3$ obtained via the reduction of CuCl_2 under NH_3 at elevated temperatures were converted into cubic Cu_3N under $\text{NH}_3: \text{O}_2$ at a lower temperature without exposure of the Cu to the ambient. The Cu_3N layers on $m\text{-Al}_2\text{O}_3$ have an anti- ReO_3 cubic crystal structure with a lattice constant of 3.8 \AA and are n-type with carrier density $n = 2 \times 10^{16} \text{ cm}^{-3}$ and mobility $\mu_n = 32 \text{ cm}^2/\text{Vs}$ at room temperature. The electrical properties are described in conjunction with theoretical calculations of the conduction band potential profile, surface band bending and depletion in the effective mass approximation.

2. Materials and Methods

Initially, 1.34 mg of CuCl_2 (Aldrich 99.999%, 134.45 gmol^{-1}), which has a rusty-brown color, was dissolved in 100 mL ethanol $\text{CH}_3\text{CH}_2\text{OH}$ and stirred at 1000 rpm for 10 min

at room temperature. CuCl_2 is soluble in water (75 g/100 mL H_2O at 25 °C) and ethanol (53 g/100 mL $\text{CH}_3\text{CH}_2\text{OH}$ at 25 °C) but less so in acetonitrile CH_3CN (1.6 g/100 mL at 20 °C). In contrast, CuCl has a considerably lesser solubility than that of CuCl_2 . More specifically, CuCl is slightly soluble in water (0.0047 g/100 mL H_2O at 20 °C) and insoluble in ethanol $\text{CH}_3\text{CH}_2\text{OH}$ and acetone $(\text{CH}_3)_2\text{CO}$. In order to obtain a satisfactory growth rate, a 0.1 M solution of CuCl_2 in $\text{CH}_3\text{CH}_2\text{OH}$ was prepared that has a dark green color due to the $(\text{CuCl}_4)^{2-}$ ions that are yellow and Cu^{+2} ions that are blue. The 0.1 M CuCl_2 liquid precursor was turned into a mist using a Venturi nebulizer and Ar as a carrier gas. Square samples of $\sim 8 \text{ mm} \times 8 \text{ mm}$ m- Al_2O_3 with a thickness of $\sim 0.3 \text{ mm}$ were cleaned sequentially in trichloroethylene, methanol, acetone and isopropanol at 80 °C, after which they were rinsed in deionized water at 20 °C and dried with nitrogen, followed by a dehydration bake at 120 °C. The clean m- Al_2O_3 was loaded in a quartz boat that was positioned at the center of a 1" hot wall, single zone AACVD reactor, capable of reaching 1100 °C that was fed by a manifold consisting of four mass flow controllers connected to Ar, NH_3 , O_2 and H_2 and a separate side manifold for controlling the flow of Ar through the Venturi nebulizer, as shown in Figure 1a. The reactor was purged with 1000 mL/min of Ar for 10 min from the main manifold, after which the temperature was ramped at 30 °C/min under a flow of 90 mL/min Ar: 10 mL/min H_2 at one atmosphere. Upon reaching 600 °C, the flow of Ar: H_2 was interrupted and a flow of 800 mL/min NH_3 was initiated, while at the same time a flow of 1000 mL/min Ar was established through the nebulizer. A visible flow of the aerosol was observed on the upstream side that was maintained for 30 min. Subsequently, the flow of Ar through the Venturi nebulizer was interrupted and the reactor allowed to cool down to 400 °C under a flow of 300 mL min^{-1} NH_3 . Upon reaching 400 °C, the Cu was converted into Cu_3N under a flow of 300 mL min^{-1} NH_3 and 15 mL min^{-1} O_2 for 30 min. At the end of the growth period, cool down took place under a flow of 300 mL/min NH_3 supplied from the main manifold until the temperature fell below 100 °C. A typical temperature–time profile is shown in Figure 1b. The Cu_3N layers were removed after purging with 1000 mL min^{-1} of Ar at room temperature and were stored in a desiccator under vacuum.

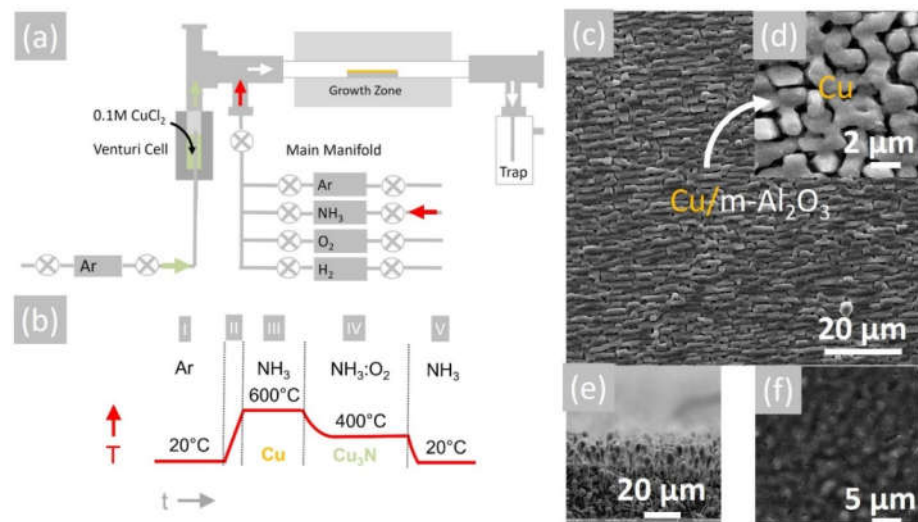


Figure 1. (a) Schematic of 1" AACVD hot wall-reactor; (b) temperature–time profile for the deposition of Cu and conversion to Cu_3N (c); (d) SEM image of Cu on m- Al_2O_3 obtained at 600 °C showing ordering of the grains; (e) side view of SEM image of Cu on m- Al_2O_3 obtained at 600 °C showing columnar growth; (f) SEM image of Cu_3N obtained from Cu under NH_3 : O_2 at 400 °C.

The morphology and crystal structure of the Cu_3N layers were determined by scanning electron microscopy (SEM) and X-ray diffraction (XRD). The carrier density and mobility of the Cu_3N layers were determined by the Hall effect in the van der Pauw configuration

by using a Keithley 2635A constant current source in conjunction with a Keithley 2182 voltmeter controlled by LabView.

3. Results and Discussion

The reaction of CuCl_2 in $\text{CH}_3\text{CH}_2\text{OH}$ with an excess of NH_3 did not lead to the direct deposition of Cu_3N , as in the case of HVPE of III-V semiconductors such as $\text{In}_x\text{Ga}_{1-x}\text{N}$, but resulted into the deposition of metallic Cu on $m\text{-Al}_2\text{O}_3$ that had a shiny, reflective surface and metallic conductivity. A typical SEM image of the Cu layer obtained on $m\text{-Al}_2\text{O}_3$ at 600°C is shown in Figure 1c, from which one may observe that the Cu layer is polycrystalline and consists of grains oriented along a single direction. A higher magnification image is also shown in Figure 1d, from which it is evident that the grains have sizes of $\sim 5\ \mu\text{m}$, while a side view of the Cu on $m\text{-Al}_2\text{O}_3$ is shown in Figure 1e, showing that columnar growth occurs. The epitaxial growth of Cu on $c\text{-Al}_2\text{O}_3$ and $a\text{-Al}_2\text{O}_3$ has been investigated extensively for the growth of high-quality graphene [24,25], but only a few have considered the growth of Cu on $m\text{-Al}_2\text{O}_3$ [26]. The deposition of Cu on $m\text{-Al}_2\text{O}_3$, which contains grooves or steps along specific crystallographic directions, as shown in Figure 2a, will lead to instabilities and ruptures of the Cu layer at elevated temperatures [27]. These ruptures occur at high curvature sites, i.e., peaks and ridges, which act as retracting edges leading to a net flux of atoms away from the high positive curvature regions. For sufficiently thin layers, this process will lead to a self-assembly of the Cu grains along a specific direction [28].

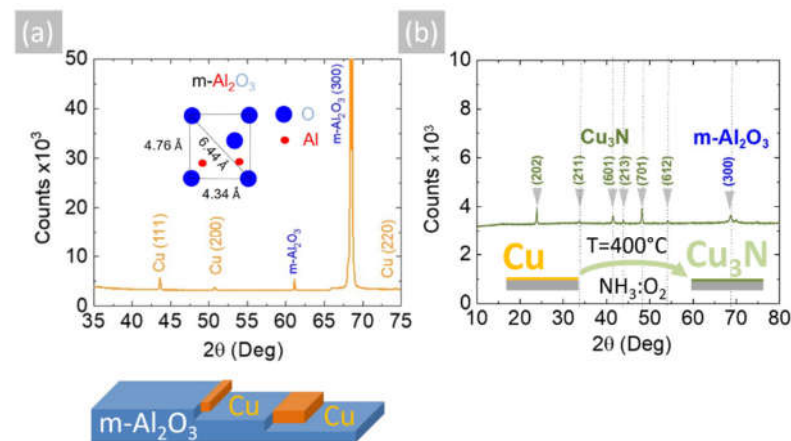


Figure 2. (a) XRD of Cu on $m\text{-Al}_2\text{O}_3$ obtained at 600°C showing peaks belonging to Cu and $m\text{-Al}_2\text{O}_3$; inset shows the oxygen-terminated surface of $m\text{-Al}_2\text{O}_3$; (b) XRD of Cu_3N obtained from Cu under $\text{NH}_3:\text{O}_2$ at 400°C showing the peaks belonging to the anti- ReO_3 cubic crystal structure of Cu_3N and $m\text{-Al}_2\text{O}_3$.

The Cu layers exhibited clear peaks in the XRD, as shown in Figure 2a, corresponding to the face-centered cubic (fcc) crystal structure of Cu with a lattice constant of $3.6\ \text{\AA}$. No peaks belonging to CuO , Cu_4O_3 or Cu_2O are observed in Figure 2a. Likewise shown are the peaks corresponding to the underlying $m\text{-Al}_2\text{O}_3$, which has an oxygen-terminated surface with tetragonal crystal symmetry that is suitable for the epitaxial growth of semiconductors with a cubic crystal structure. It is worthwhile to point out that the deposition of Cu on $n\text{-type Si (001)}$ resulted in columnar growth, as shown in Figure 3a,b. The Cu pillars have a height of $\sim 20\ \mu\text{m}$, but they are not ordered in any way. No Cu_3N was obtained under an excess of NH_3 by varying the temperature between 300°C and 800°C . Instead, the reaction of CuCl_2 in $\text{CH}_3\text{CH}_2\text{OH}$ with NH_3 always led to the deposition of Cu on $m\text{-Al}_2\text{O}_3$, which occurs via the reduction of CuCl_2 to CuCl and then into Cu by the H_2 evolving from NH_3 .

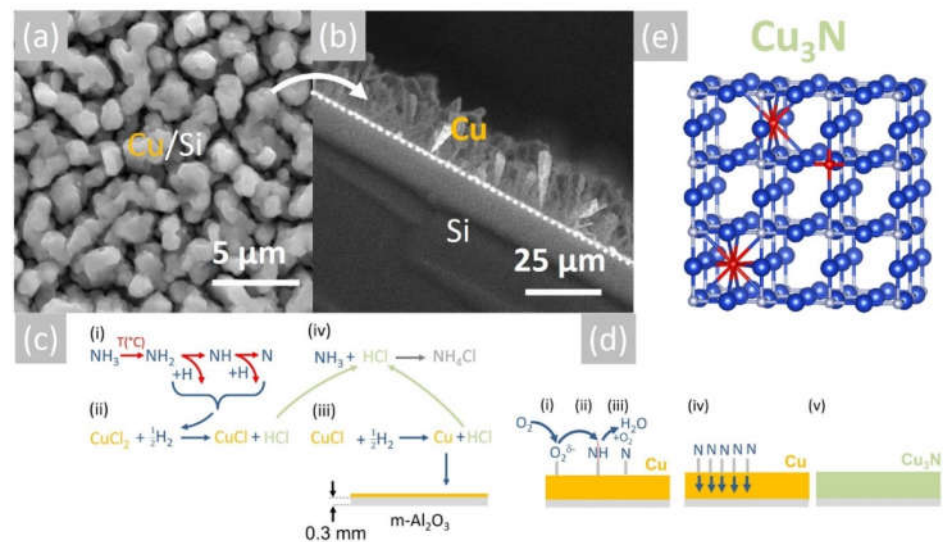


Figure 3. (a) SEM image of Cu on Si obtained at 600 °C and (b) section showing the formation of Cu rods on Si; (c) reaction mechanism for the deposition of Cu and (d) reaction mechanism for the conversion of Cu into Cu_3N obtained under NH_3 : O_2 ; (e) stick and ball model of the anti- ReO_3 cubic crystal structure of Cu_3N ; large blue spheres (Cu), small grey spheres (N) and red spheres (O).

More specifically, the 0.1 M solution of CuCl_2 is initially converted into a mist of liquid drops and mixed with NH_3 , which is soluble in $\text{CH}_3\text{CH}_2\text{OH}$ [29]. Subsequently, the liquid drops are vaporized at an elevated temperature, and the $\text{CH}_3\text{CH}_2\text{OH}$ gives C_2H_4 and H_2O according to the reaction $\text{C}_2\text{H}_5\text{OH} \rightarrow \text{C}_2\text{H}_4 + \text{H}_2\text{O}$. No carbon is released from the pyrolysis of C_2H_4 between 500 °C and 800 °C [30]. Upon vaporization, CuCl_2 , which has a melting point of 498 °C, will be reduced to CuCl , which has an even lower melting point of 423 °C [31], and finally into metallic Cu by the H_2 evolving from the breakdown of NH_3 . Before elaborating further, it is useful to note that the thermal breakdown of NH_3 into N_2 and H_2 was investigated as early as 1905 by White et al. [32], who showed that it depends on the gas flow, i.e., residence time as well as the temperature. In particular, White et al. [32] showed that a flow of 200 mL/min NH_3 resulted in a dissociation of 5% NH_3 at 600 °C and 10% at 700 °C. However, the breakdown of NH_3 is also promoted catalytically by the deposited Cu at elevated temperatures [33]. In other words, the Cu deposited on the $m\text{-Al}_2\text{O}_3$ will participate actively in the dissociation of NH_3 near the surface, thereby further promoting the reduction of CuCl_2 and deposition of Cu, which has a melting point of 1085 °C. A schematic representation of the proposed reaction mechanism is shown in Figure 3c. For completeness, it must also be pointed out that the NH_3 will react with $\text{CH}_3\text{CH}_2\text{OH}$ and give ethylamine ($\text{CH}_3\text{CH}_2\text{NH}_2$) and acetonitrile (CH_3CN), which have boiling points of 20 °C and 82 °C, respectively. $\text{CH}_3\text{CH}_2\text{NH}_2$ and CH_3CN will dissociate into HCN and CH_4 depending on the temperature and residence time, but they are not expected to influence the overall reaction governing the deposition of Cu. It is also important to mention that the Cu will tend to react with H_2O supplied from the $\text{CH}_3\text{CH}_2\text{OH}$ and give CuO and Cu_2O . However, no oxides are detected in Figure 2a, so it is very likely that they are reduced to metallic Cu due to the H_2 evolving from the NH_3 over the Cu. This is consistent with the findings of Kim et al. [34], who showed that CuO is converted into metallic Cu under an excess of H_2 without the formation of intermediate Cu_4O_3 or Cu_2O .

In short, CuCl_2 is reduced to CuCl and then into Cu by the H_2 evolving from NH_3 , according to: $\text{CuCl}_2 + \text{H}_2 \rightarrow \text{CuCl} + 2\text{HCl}$ and $2\text{CuCl} + \text{H}_2 \rightarrow 2\text{Cu} + 2\text{HCl}$. The HCl reacted in turn with the excess NH_3 , giving NH_4Cl , i.e., $\text{NH}_3 + \text{HCl} \rightarrow \text{NH}_4\text{Cl}$, which solidified below its sublimation temperature, i.e., ~340 °C near the cool end of the reactor, very similar to what occurs during conventional HVPE of III-Vs.

The reduction of CuCl_2 into Cu may also be achieved by using H_2 as opposed to NH_3 . In order to show this, the 0.1 M solution of CuCl_2 in $\text{CH}_3\text{CH}_2\text{OH}$ was used to deposit a layer of CuCl_2 on 15 mm \times 30 mm soda lime glass (SLG) slides by drop-casting, as shown in Figure 4a. The CuCl_2 layer had a light green color and good uniformity, and a typical SEM image is shown in Figure 4b. This was converted into Cu under a flow of (i) 10 and (ii) 50 mL \cdot min $^{-1}$ pure H_2 at 400 °C for 30 min, as shown schematically in Figure 4c. The CuCl_2 as-deposited on SLG displayed a crystalline structure and multiple peaks in the XRD, as shown in Figure 4d, but all the peaks were eliminated after the reduction of the CuCl_2 into Cu.

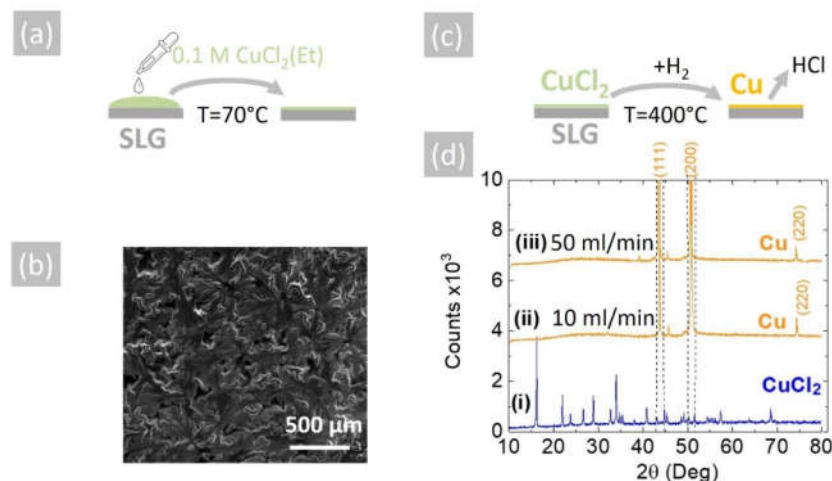


Figure 4. (a) Schematic illustration of drop-casting a 0.1 M CuCl_2 (Et) solution on SLG at 70 °C to aid the evaporation of the ethanol; (b) SEM image of the CuCl_2 on SLG, which had a light green color; (c) schematic of conversion of CuCl_2 into Cu under H_2 at 400 °C; (d) XRD of (i) CuCl_2 as-deposited on SLG, (ii) Cu obtained from CuCl_2 under 10 mL/min H_2 and (iii) 50 mL/min H_2 . All of the CuCl_2 peaks vanish, and the peaks belonging to Cu do not overlap with those of CuCl_2 , as shown with the aid of the broken vertical lines.

The Cu deposited on m- Al_2O_3 at 600 °C by AACVD using CuCl_2 and NH_3 has a higher crystal quality compared to the Cu obtained by sputtering, which was nonetheless successfully converted into crystalline Cu_3N under a flow of 300 mL/min NH_3 and 15 mL/min O_2 between 400 °C and 600 °C, as shown previously [12]. The Cu_3N obtained in this way had an anti- ReO_3 cubic crystal structure, and we observed the M and R direct energy band gaps of Cu_3N by UPPS in excellent agreement with DFT calculations of the electronic structure, confirming that it has a clean energy gap [12]. Consequently, the polycrystalline Cu layer that was obtained by AACVD on m- Al_2O_3 at 600 °C was converted into Cu_3N under a flow of 300 mL/min NH_3 and 15 mL/min O_2 at 400 °C. The Cu_3N had an olive-green-like color, and a typical SEM image of the Cu_3N layer on m- Al_2O_3 is shown in Figure 1f. This exhibited peaks in the XRD, as shown in Figure 2b, corresponding to the anti- ReO_3 cubic crystal structure of Cu_3N with a lattice constant of 3.8 Å.

The reaction of Cu with NH_3 containing O_2 and the formation of Cu_3N can be understood by considering the catalytic oxidation of NH_3 by O_2 in the presence of a catalyst, e.g., Cu, Pt, etc., at elevated temperatures, as described by Carley et al. [35], who investigated the catalytic reactivity of Cu (110) metal surfaces with coadsorbed NH_3 and O_2 . More specifically, Carley et al. [35] proposed that the oxidation of NH_3 leads to the formation of a stabilized N monolayer on the Cu metal surface, which in turn is responsible for the conversion of the bulk Cu layer into Cu_3N . It should be noted that the reaction of NH_3 with O_2 also gives H_2O according to the reaction $\text{NH}_3 + \text{O}_2 \rightarrow \text{NO} + \text{H}_2\text{O}$, which was observed to condense near the cool end of the reactor upon increasing the gas flow of O_2 . The reaction mechanism of the conversion of Cu into Cu_3N is depicted schematically in Figure 3d. No Cu_3N was obtained from Cu by using only NH_3 , in accordance with

Matsuzaki et al. [15]. Moreover, no CuO or Cu₂O peaks are detected in Figure 2b, but Cu₂O will nevertheless form as native oxide on the surface of the Cu₃N upon exposure to the ambient, as we have shown previously by using Raman spectroscopy [36]. Before considering the electrical properties of the Cu₃N layers, it is useful to point out that the reaction of CuCl₂ with a smaller flow of 100 mL/min NH₃ at 600 °C mainly led to the deposition of Cu₂O, not Cu₃N.

In order to measure the Hall effect, Ag ohmic contacts were deposited at the four corners of the Cu₃N layers on m-Al₂O₃. It has been shown that Au, Ag and Cu in Cu₃N give rise to a semiconductor-to-metal transition and remarkably constant electrical resistivity over a very broad range of temperatures [37]. Consequently Ag, Au and Cu may be used for the formation of ohmic contacts on Cu₃N, and in the past, we have shown that Au and Ag deposited on n-type Cu₃N results in the formation of contacts with linear IVs [13]. The Cu₃N layers on m-Al₂O₃ were found to be n-type and had room temperature carrier densities of $2 \times 10^{16} \text{ cm}^{-3}$ with a maximum mobility of 32 cm²/Vs. The Cu₃N layers are n-type as they are Cu-rich, but also due to the fact that oxygen may be included in the Cu₃N by the preferential formation of interstitial oxygen (O_i) that acts as donors, not as acceptors [36]. Furthermore, the Cu₃N layers obtained here were found to be persistently n-type, and the carrier density and mobility did not exhibit any changes upon illumination with light of $\lambda = 450 \text{ nm}$ under ambient conditions. In other words, the n-type Cu₃N layers did not exhibit any photoconductivity, which may be attributed to recombination via Cu_i and V_N states, in accordance with Yee et al. [1].

It is worthwhile pointing out here that Matsuzaki et al. [15] showed that epitaxial Cu₃N layers with a thickness of 25 nm on SrTiO₃ were p-type, due to the upward surface band bending mediated by the chemisorption of O₂[−], but switched to n-type upon exposure to ultraviolet (UV) light and reverted back to p-type after terminating the irradiation. In contrast, they observed that the Cu₃N layers remained n-type after exposure to UV light under vacuum, confirming that the adsorbed O₂[−] is responsible for the surface inversion observed under ambient conditions in air. However, the epitaxial Cu₃N layers of Matsuzaki et al. [15] were found to be persistently n-type under ambient conditions, with a carrier density of the order of 10^{14} cm^{-3} and mobility of 100 cm²/Vs after annealing under NH₃ between 125 and 350 °C, suggesting a change in the composition of the surface and overall band bending. The Cu₃N layers obtained here were found to be persistently n-type and had a room temperature carrier density of $2 \times 10^{16} \text{ cm}^{-3}$, perhaps due to the fact that after the conversion of Cu into Cu₃N under NH₃: O₂, the flow of NH₃ was maintained for at least 30 min until the temperature fell well below 100 °C.

However, the properties of Cu₃N layers with a thickness of a few tens of nm will depend strongly on the properties of the surface but also the properties of the underlying substrate that is often overlooked. The Cu₃N layers obtained here are persistently n-type with a carrier density of $2 \times 10^{16} \text{ cm}^{-3}$, most likely due to the fact that the thickness of the Cu₃N layers is greater than 1 μm, so it is bulk-like and will not be strongly influenced by properties of the surface or underlying m-Al₂O₃. In thermodynamic equilibrium, the Fermi level (E_F) with respect to the conduction band minimum (E_C) away from the surface and deep in the bulk is determined from:

$$n = N_C e^{-\frac{E_C - E_F}{kT}},$$

where N_C is the conduction band effective density of states, k is Boltzmann's constant and T the temperature taken to be equal $T = 300 \text{ K}$. The electron density is equal to $n = 2 \times 10^{16} \text{ cm}^{-3}$, and the conduction band effective density of states in Cu₃N is given by:

$$N_C = 2 \left(\frac{2\pi m_n kT}{h^2} \right)^{\frac{3}{2}},$$

where m_n is the electron effective mass in Cu_3N taken to be $m_n = 0.16 m_0$ [6], m_0 is the free-electron mass and h is Planck's constant. This gives $N_C = 1.6 \times 10^{24} \text{ m}^{-3}$ or $1.6 \times 10^{18} \text{ cm}^{-3}$, so $E_C - E_F = 0.11 \text{ eV}$ in the bulk where a flat band condition exists. On the other hand, the energetic position of the Fermi level with respect to the conduction band edge, i.e., $E_C - E_F$, at the surface is dependent on the local density and energetic position of any surface states that will be occupied by electrons, which in turn may pin the Fermi level at the surface. According to Navío et al. [38], the Fermi level at the surface of ultrathin Cu_3N layers is pinned at the middle of the gap, which will give rise to a barrier height of $\phi_b = 0.5 \text{ eV}$. The surface depletion region will extend into the Cu_3N , and the depletion width is:

$$w = \sqrt{\frac{2\epsilon_s \phi_b}{eN_D}},$$

where $\epsilon_s = \epsilon_R \epsilon_0$, ϵ_R is the static dielectric constant of Cu_3N , ϵ_0 the permittivity of free space, e the electron charge and N_D the donor density taken to be equal to $n = 2 \times 10^{16} \text{ cm}^{-3}$. Considering that the static dielectric constant of Cu_3N is $\epsilon_R \sim 10$ [39], the depletion width is found to be $w = 0.16 \text{ }\mu\text{m}$, taking into account that the Fermi level at the surface of Cu_3N layers is pinned at the middle of the gap, according to Navío et al. [38]. However, despite the fact that we did not detect any CuO or Cu_2O in the XRD, a thin layer of Cu_2O will exist on the surface of Cu_3N . According to Hodby et al. [40], the Fermi level at the surface of Cu_2O is pinned at states residing energetically in the upper half of the band gap $\sim 0.4 \text{ eV}$ below the conduction band edge. The native Cu_2O layer of Cu_3N is expected to have a thickness of only a few nm and will be completely depleted, so the depletion width taking $\phi_b = 0.4 \text{ eV}$ is found to be $w = 0.15 \text{ }\mu\text{m}$. The conduction band potential profile of the Cu_3N layer including the native Cu_2O layer at its surface is shown in Figure 5a, where the work function and electron affinity of Cu_3N i.e., $\phi(\text{Cu}_3\text{N}) = 5.0 \text{ eV}$ and $\chi(\text{Cu}_3\text{N}) = 3.5 \text{ eV}$ [41] have been considered as well as the work function and electron affinity of Cu_2O , i.e., $\phi(\text{Cu}_2\text{O}) = 4.8 \text{ eV}$ and $\chi(\text{Cu}_2\text{O}) = 3.2 \text{ eV}$ [42]. The formation of p-type Cu_2O over the n-type Cu_3N will lead to the confinement of photogenerated electron-hole pairs at the $\text{Cu}_2\text{O}/\text{Cu}_3\text{N}$ heterojunction, which will inadvertently result into recombination via states at the interface, thereby suppressing the photoconductivity. This mechanism is different to that put forward by Yee et al. [1], who fabricated an Al: ZnO/ZnS/ Cu_3N p-n heterojunction that exhibited rectifying behavior but no photogenerated current, which was attributed to the large concentration of Cu_i defects that capture electrons and result in substantial Shockley-Read-Hall recombination and quenching of the steady-state minority carrier concentration under illumination. While it is possible that both mechanisms are responsible for the suppression of the photocurrent and photoconductivity in Cu_3N , it is imperative that the surface recombination should be suppressed via the deposition of suitable layers that prevent the formation of Cu_2O that was originally suggested to act as a suitable passivation layer for Cu_3N , similar to that of SiO_2 for Si p-n junction solar cells [2].

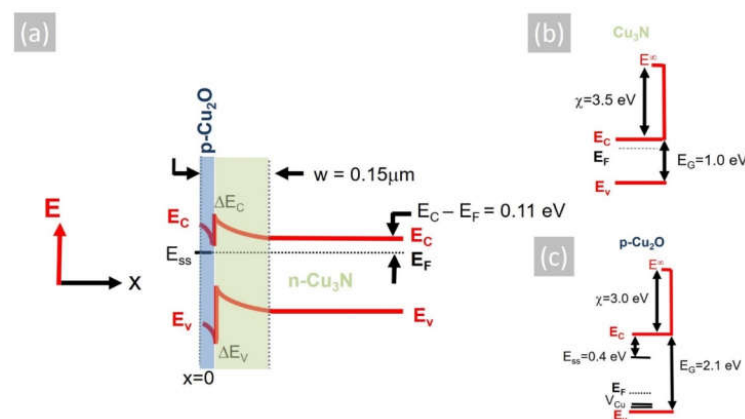


Figure 5. (a) Energy band potential profile of a $\text{Cu}_2\text{O}/\text{Cu}_3\text{N}$ p-n heterojunction consisting of n-type Cu_3N and the native, surface p-type Cu_2O , where the Fermi level (E_F) is pinned at the surface states

(E_{ss}) residing ~ 0.4 eV below the conduction band edge of Cu_2O ; also shown are the conduction (ΔE_C) and valence (ΔE_V) band discontinuities as well as the surface depletion w that extends 0.15 μm through the p-type Cu_2O and into the n-type Cu_3N . (b) Energy band diagram of n-type Cu_3N showing the conduction (E_C) and valence (E_V) bands as well as the Fermi level (E_F) and electron affinity (χ) of Cu_3N , (c) same for Cu_2O ; also shown are the (V_{Cu}) acceptor states, which reside above the top of the valence band, and the energetic position of the surface states (E_{ss}).

4. Conclusions

Cu_3N layers have been grown on m- Al_2O_3 by aerosol-assisted chemical vapor deposition using 0.1 M CuCl_2 in $\text{CH}_3\text{CH}_2\text{OH}$ under an excess of NH_3 at 600 °C, which resulted in the deposition of epitaxial Cu layers consisting of oriented grains with a face-centered cubic crystal structure that were subsequently converted into Cu_3N under NH_3 : O_2 at 400 °C in a two-step process without exposure to the ambient. The reaction of CuCl_2 with an excess of NH_3 did not give Cu_3N , which is different to halide vapor phase epitaxy of III-V semiconductors such as $\text{In}_x\text{Ga}_{1-x}\text{N}$. The Cu_3N layers obtained in this way have an anti- ReO_3 cubic crystal structure and persistent room temperature carrier density of $n = 2 \times 10^{16} \text{ cm}^{-3}$ and mobility of $\mu_n = 32 \text{ cm}^2/\text{Vs}$, but they did not exhibit any photoconductivity due to recombination via surface states in the Cu_2O or via indirect recombination via Cu_i defects, which capture electrons and result into substantial Shockley–Read–Hall recombination

Funding: This research received no external funding.

Institutional Review Board Statement: Not applicable.

Informed Consent Statement: Not applicable.

Conflicts of Interest: The author declares no conflict of interest.

References

1. Yee, Y.S.; Inoue, H.; Hultqvist, A.; Hanifi, D.; Salleo, A.; Magyari-Köpe, B.; Nishi, Y.; Bent, S.F.; Clemens, B.M. Copper Interstitial Recombination Centers in Cu_3N . *Phys. Rev. B* **2018**, *97*, 245201. [[CrossRef](#)]
2. Zakutayev, A. Defect Tolerant Semiconductors for Solar Energy Conversion. *J. Phys. Chem. Lett.* **2014**, *5*, 1117–1125. [[CrossRef](#)] [[PubMed](#)]
3. Chen, S.C.; Huang, S.Y.; Sakalley, S.; Paliwal, A.; Chen, Y.H.; Liao, M.H.; Sun, H.; Biring, S. Optoelectronic Properties of Cu_3N Thin Films Deposited by Reactive Magnetron Sputtering and its Diode Rectification Characteristics. *J. Alloys Compd.* **2019**, *789*, 428–434. [[CrossRef](#)]
4. Juza, R.; Hahn, H. Über die Kristallstrukturen von Cu_3N , GaN und InN . *Z. Anorg. Chem.* **1938**, *239*, 282–287. [[CrossRef](#)]
5. Suwannatus, S.; Duangsawat, B.; Pakdee, U. Lithium Storage Performance of Copper Nitride Films Deposited by Reactive DC Magnetron Sputtering. *Mater. Today Proc.* **2018**, *5*, 15208–15212. [[CrossRef](#)]
6. Birkett, M.; Savory, C.N.; Fioretti, A.N.; Thompson, P.; Muryn, C.A.; Weerakkody, A.D.; Mitrovic, I.Z.; Hall, S.; Treharne, R.; Dhanak, V.R.; et al. Atypically Small Temperature-Dependence of the Direct Band Gap in the Metastable Semiconductor Copper Nitride Cu_3N . *Phys. Rev. B* **2017**, *95*, 115201. [[CrossRef](#)]
7. Matsuzaki, K.; Okazaki, T.; Lee, Y.S.; Hosono, H.; Susaki, T. Controlled Bipolar Doping in Cu_3N (100) Thin Films. *Appl. Phys. Lett.* **2014**, *105*, 222102. [[CrossRef](#)]
8. Park, J.M.; Jin, K.; Han, B.; Kim, M.J.; Jung, J.; Kim, J.J.; Lee, W.J. Atomic layer Deposition of Copper Nitride Film and its Application to Copper Seed Layer for Electrodeposition. *Thin Solid Film.* **2014**, *556*, 434–439. [[CrossRef](#)]
9. Li, Z.; Gordon, R.G. Thin, Continuous, and Conformal Copper Films by Reduction of Atomic Layer Deposited Copper Nitride. *Chem. Vap. Depos.* **2006**, *12*, 435–441. [[CrossRef](#)]
10. Gallardo-Vega, C.; de la Cruz, W. Study of the Structure and Electrical Properties of the Copper Nitride Thin Films Deposited by Pulsed Laser Deposition. *Appl. Surf. Sci.* **2006**, *252*, 8001–8004. [[CrossRef](#)]
11. Soto, G.; Diaz, J.A.; de la Cruz, W. Copper Nitride Films Produced by Reactive Pulsed Laser Deposition. *Mater. Lett.* **2003**, *57*, 4130–4133. [[CrossRef](#)]
12. Zervos, M.; Othonos, S.; Sergides, M.; Pavludis, T.; Kioseoglou, J. Observation of the Direct Energy Band Gaps of Defect-Tolerant Cu_3N by Ultrafast Pump-Probe Spectroscopy. *J. Phys. Chem. C* **2020**, *124*, 3459–3469. [[CrossRef](#)]
13. Tilemachou, A.; Zervos, M.; Othonos, A.; Pavludis, T.; Kioseoglou, J. p-type Iodine Doping of Cu_3N and its Conversion to γ - CuI for the Fabrication of γ - $\text{CuI}/\text{TiO}_2/\text{Cu}_3\text{N}$ p-n Heterojunctions. *J. Electron. Mater.* **2022**, *3*, 15–26. [[CrossRef](#)]

14. Gao, L.; Jin, A.L.; Zhang, W.B.; Cao, Z.X. Insertion of Zn Atoms into Cu₃N Lattice: Structural Distortion and Modification of Electronic Properties. *J. Cryst. Growth* **2011**, *321*, 157–161. [[CrossRef](#)]
15. Matsuzaki, K.; Harada, K.; Kumagai, Y.; Koshiya, S.; Kimoto, K.; Ueda, S.; Sasase, M.; Maeda, A.; Susaki, T.; Kitano, M.; et al. High-Mobility p-Type and n-Type Copper Nitride Semiconductors by Direct Nitriding Synthesis and In Silico Doping Design. *Adv. Mater.* **2018**, *30*, 1801968. [[CrossRef](#)] [[PubMed](#)]
16. Ahn, D.; Park, S.H. Cuprous Halides Semiconductors as a New Means for Highly Efficient Light-Emitting Diodes. *Sci. Rep.* **2016**, *6*, 20718. [[CrossRef](#)]
17. Marchand, P.; Hassan, I.A.; Parkin, I.P.; Carmalt, C.J. Aerosol-Assisted Delivery of Precursors for Chemical Vapor Deposition: Expanding the Scope of CVD for Materials Fabrication. *Dalton Trans.* **2013**, *42*, 9406. [[CrossRef](#)]
18. Knapp, C.E.; Carmalt, C.J. Solution Based CVD of Main Group Materials. *Chem. Soc. Rev.* **2016**, *45*, 1036. [[CrossRef](#)]
19. McInnes, A.; Sagu, J.S.; Mehta, D.; Wijayantha, K.G.U. Low-Cost Fabrication of Tunable Band Gap Composite Indium and Gallium Nitrides. *Sci. Rep.* **2019**, *9*, 2313. [[CrossRef](#)]
20. Jeong, Y.S.; An, S.H.; Shin, C.H. Selective Synthesis of Acetonitrile by Reaction of Ethanol with Ammonia Over Ni/Al₂O₃ Catalyst. *Korean J. Chem. Eng.* **2019**, *36*, 1051–1056. [[CrossRef](#)]
21. Metcalfe, E.; Booth, D.; McAndrew, H.; Woolley, W.D. The Pyrolysis of Organic Nitriles. *Fire Mater.* **1983**, *7*, 185–192. [[CrossRef](#)]
22. Asmus, T.W.; Houser, T.J. Pyrolysis Kinetics of Acetonitrile. *J. Phys. Chem.* **1969**, *73*, 2555–2558. [[CrossRef](#)]
23. Yamaguchi, T.; Nagai, H.; Kiguchi, T.; Wakabayashi, N.; Igawa, T.; Hitora, T.; Onuma, T.; Honda, T.; Sato, M. Epitaxial Mist Chemical Vapor Deposition Growth and Characterization of Cu₃N Films on (0001) α -Al₂O₃ Substrates. *Appl. Phys. Express* **2020**, *13*, 075505. [[CrossRef](#)]
24. Verguts, K.; Vermeulen, B.; Vrancken, N.; Schouteden, K.; Haesendonck, C.; Huyghebaert, C.; Heyns, M.; Gendt, S.; Brems, S. Epitaxial Al₂O₃(0001)/Cu (111) Template Development for CVD Graphene Growth. *J. Phys. Chem. C* **2016**, *120*, 297–304. [[CrossRef](#)]
25. Miller, D.; Keller, M.W.; Shaw, J.M.; Chiaramonti, A.N.; Keller, R.R. Epitaxial (111) Films of Cu, Ni, and Cu_xNi_y on α -Al₂O₃ (0001) for Graphene Growth by Chemical Vapor Deposition. *J. Appl. Phys.* **2012**, *112*, 064317. [[CrossRef](#)]
26. Chatain, D.; Curitto, S.; Wynblatt, P.; Meltzman, H.; Kaplan, W.D.; Rohrer, G.S. Orientation Relationships of Copper Crystals on Sapphire (1 0 1 0) m-Plane and (1 0 1 2) r-Plane Substrates. *J. Cryst. Growth* **2015**, *418*, 57–63. [[CrossRef](#)]
27. Hughes, R.A.; Menumerov, E.; Neretina, S. When Lithography Meets Self-Assembly: A Review of Recent Advances in the Directed Assembly of Complex Metal Nanostructures on Planar and Textured surfaces. *Nanotechnology* **2017**, *28*, 282002. [[CrossRef](#)]
28. Giermann, A.L.; Thompson, C.V. Solid-state Dewetting for Ordered Arrays of Crystallographically Oriented Metal Particles. *Appl. Phys. Lett.* **2005**, *86*, 121903. [[CrossRef](#)]
29. Huang, L.J.; Xue, W.L.; Zeng, Z.X. The Solubility of Ammonia in Ethanol between 277.35 K and 328.15 K. *Fluid Phase Equilib.* **2001**, *303*, 80–84. [[CrossRef](#)]
30. Ruiz, M.P.; Callejas, A.; Millera, A.; Alzueta, M.U.; Bilbao, R. Soot Formation from C₂H₂ and C₂H₄ Pyrolysis at Different Temperatures. *J. Anal. Appl. Pyrolysis* **2007**, *79*, 244–251. [[CrossRef](#)]
31. Proust, J.L. Recherches sur le Cuivre'. *Ann. Chim. Phys.* **1799**, *32*, 26–54.
32. White, A.H.; Melville, W. The Decomposition of Ammonia at High Temperatures. *J. Am. Chem. Soc.* **1905**, *27*, 373–386. [[CrossRef](#)]
33. Bao, J.L.; Carter, E.A. Surface-Plasmon-Induced Ammonia Decomposition on Copper: Excited-State Reaction Pathways Revealed by Embedded Correlated Wavefunction Theory. *ACS Nano* **2019**, *13*, 9944–9957. [[CrossRef](#)] [[PubMed](#)]
34. Kim, J.Y.; Rodriguez, J.A.; Hanson, J.C.; Frenkel, A.I.; Lee, P.L. Reduction of CuO and Cu₂O with H₂: H Embedding and Kinetic Effects in the Formation of Suboxides. *J. Am. Chem. Soc.* **2003**, *125*, 10684–10692. [[CrossRef](#)] [[PubMed](#)]
35. Carley, A.F.; Davies, P.R.; Roberts, M.W. Activation of Oxygen at Metal Surfaces. *Philos. Trans. R. Soc. A* **2005**, *363*, 829–846. [[CrossRef](#)]
36. Zervos, M.; Othonos, A.; Pavloutidis, T.; Giaremis, S.; Kioseoglou, J.; Mavridou, K.; Katsikini, M.; Pinakidou, F.; Paloura, E.C. Impact of Oxygen on the Properties of Cu₃N and Cu_{3-x}N_{1-x}O_x. *J. Phys. Chem. C* **2021**, *125*, 3680–3688. [[CrossRef](#)]
37. Lu, N.; Ji, A.; Cao, Z. Nearly Constant Electrical Resistance Over Large Temperature Range in Cu₃NM_x (M = Cu, Ag, Au) Compounds. *Sci. Rep.* **2013**, *3*, 3090. [[CrossRef](#)]
38. Navío, C.; Capitán, M.J.; Álvarez, J.; Yndurain, F.; Miranda, R. Intrinsic Surface Band Bending in Cu₃N (100) Ultrathin Films. *Phys. Rev. B* **2007**, *76*, 085105. [[CrossRef](#)]
39. Kim, K.J.; Kim, J.H.; Kang, J.H. Structural and Optical Characterization of Cu₃N Films Prepared by Reactive RF Magnetron Sputtering. *J. Cryst. Growth* **2001**, *222*, 767–772. [[CrossRef](#)]
40. Hodby, J.W.; Jenkins, T.E.; Schwab, C.; Tamura, H.; Trivich, D. Cyclotron Resonance of Electrons and of Holes in Cuprous Oxide Cu₂O. *J. Phys. C* **1976**, *9*, 1429. [[CrossRef](#)]
41. Wang, L.C.; Liu, B.H.; Su, C.Y.; Liu, W.S.; Kei, C.C.; Wang, K.W.; Perng, T.P. Electronic Band Structure and Electro Catalytic Performance of Cu₃N Nanocrystals. *ACS Appl. Nano Mater.* **2018**, *1*, 3673–3681. [[CrossRef](#)]
42. Tan, S.C.; Hsu, S.E.; Ke, W.H.; Chen, L.J.; Huang, M.H. Facet-Dependent Electrical Conductivity Properties of Cu₂O Crystals. *Nano Lett.* **2015**, *15*, 2155. [[CrossRef](#)] [[PubMed](#)]